Temperature dependence of the absorption of the R(6) manifold of the 2ν3 band of methane in air in support of the MERLIN mission

S. Vasilchenko, T. Delahaye, S. Kassi, A. Campargue, R. Armante, H. Tran, Didier Mondelain

Temperature dependence of the absorption of the R(6) manifold of the $2\nu_3$ band of methane in air in support of the MERLIN mission

S. Vasilchenko[a], T. Delahaye[b], S. Kassi[a], A. Campargue[a], R. Armante[b], H. Tran[b], D. Mondelain[a,*]

[a] *Univ. Grenoble Alpes, CNRS, LIPhy, 38000 Grenoble, France*

[b] *Laboratoire de Météorologie Dynamique, IPSL, CNRS, Ecole polytechnique, Université Paris-Saclay, Palaiseau, France*

[*] Corresponding author: didier.mondelain@univ-grenoble-alpes.fr; LIPhy, Bat. E, 140 rue de la Physique, 38400 Saint-Martin d'Hères (France).

Key words

MERLIN mission; methane; CH4; line profile; temperature dependence; CRDS

Abstract

Fifty nine high sensitivity spectra of the R(6) manifold of the $2\nu_3$ band of methane in air, near 1.64 µm, have been recorded in support of the MERLIN mission. For this purpose, a cavity ring down spectrometer (CRDS) with a spectrally narrowed and stable (sub-kHz) laser source was coupled to a temperature regulated high-finesse optical cavity. The frequency scale of each spectrum was accurately determined from measurements of the beat note between a part of the laser light and the closest tooth of a frequency comb referenced to a rubidium clock. Series of spectra were recorded between 243 and 313 K with a 10 K temperature step. For each series, total pressure values of 50, 100, 250, 500 and 750 Torr were adopted. A multi-spectrum fitting procedure with the Hartmann-Tran (HT) line profile, including the first-order line-mixing parameter, has been used to derive the spectroscopic parameters for each of the six R(6) components, along with the temperature dependence of the line-shape parameters. The results show that the fitted model is able to reproduce the experimental spectra with a relative precision better than 0.2% for the entire R(6) manifold spectral region and better than 0.05% at the ON-line position of the MERLIN mission for the 250, 500 and 750 Torr spectra. The relative precision increases to 0.3% and the residuals at the ON-line position to 0.1% when including the 50 and 100 Torr spectra. Comparisons with ground-based atmospheric measurements show that these data significantly improve the modeling of methane absorption in this spectral region. We propose here a new complete line list of the methane spectrum in the region of the R(6) manifold allowing reducing notably the residuals at the ON-line position of the MERLIN mission.

1. Introduction

Atmospheric methane is the second most important anthropogenic greenhouse gas (GHG) after carbon dioxide, responsible for about 20% of the additional radiative forcing due to human activities since the industrial revolution [1]. In recent years, variations in its atmospheric concentration, reflecting the changing balance between surface emissions and atmospheric and surface sinks, have been the subject of much debate [2,3,4,5,6]. Given its short lifetime (about 9 years) compared to other major GHGs such as carbon dioxide or nitrous oxide [7], methane is a particularly appropriate target for climate change mitigation policies, which makes measuring its concentration a priority.

However, the lack of accurate measurements of atmospheric methane on a global scale is a major problem that limits our understanding of methane source and sink processes. The low spatial coverage of existing surface methane measurements does not allow for an adequate quantification of the overall distribution of methane emissions. High-precision remote sensing spatial measurements are therefore needed as a complement to achieve global coverage. In the past years, several passive remote sensors, such as SCIAMACHY [8], GOSAT [9], CarbonSat [10] and Sentinel 5 [11] have been launched to measure backscattered solar radiation from the Earth's surface as a function of wavelength. For instance, the Atmospheric Infrared Sounding Interferometer (IASI) [12], developed by the French space agency (Centre National d'Etudes Spatiales [CNES]) in collaboration with Eumetsat, and operating in the thermal infrared [13], can provide surface emissions consistent with other datasets [14], albeit with very low boundary layer sensitivity (more detail on past, current, and planned methane space mission can be found in [15] and [16]). Recently, the European Space Agency (ESA) has supported a project called ISOGG for *Improved Spectroscopy for Carbon Dioxide, Oxygen, and Water Vapour Satellite Measurement* [17] dedicated in particular to the improvement of the spectroscopic database of CH_4 in the $2\nu_3$ band near 1.64 µm region to meet the data product requirements of CO2M and Sentinel-5/UVNS.

However, passive sensors are subject to bias in regions with aerosol layers or thin ice clouds and are unable to make measurements at high latitudes during the winter months [18]. Space-based active remote sensing is therefore a complementary approach, as it can be more sensitive near the Earth's surface, has virtually no bias from aerosols and clouds, and can measure both day and night and at all latitudes.

In this context, the MEthane LIdar missioN (MERLIN), a joint French (CNES) and German (Deutsches Zentrum für Luft- und Raumfahrt [DLR]) space mission, scheduled for launch in 2027, proposes an active measurement approach to retrieve methane column-averaged dry air mole

fraction, X_{CH_4}, based on a differential absorption LIDAR (LIght Detecting And Ranging) with a nadir-integrated sighting path [16,19,20,21]. A full description of the MERLIN mission is available in [16]. The technique relies on measurements using a pulsed laser emitting at two wavelengths around 1.645 µm, one wavelength precisely locked in the middle of the methane $2\nu_3$ R(6) manifold spectral feature near 6077 cm^{-1}, and the other wavelength about 1 cm^{-1} below in a nearly absorption-free region used as a reference [16]. The main objective of the mission is to obtain spatial and temporal gradients of atmospheric methane mole fractions with high precision and unprecedented accuracy on a global scale. Specifically, the mission-breakthrough uncertainties for the measured methane mole fraction are 0.1% (or 1.9 ppb) for the systematic relative uncertainty (accuracy) and 1% for the statistical relative uncertainty (precision) at the spatial and temporal resolutions of 50 km and 1 month, respectively [20,22]. Only 30% of the systematic breakthrough error is allowed for spectroscopy (*i.e.* 0.033% on X_{CH_4}). This error has to be understood as the maximum difference caused by spectroscopic errors, between X_{CH_4} obtained for different atmospheric profiles and ground altitudes (0-2 km). Dedicated retrieval simulations done at DLR highlighted the incompliance of previous laboratory measurements with the requirements and quantified the accuracy requirements on the absorption cross-section (<0.1%), the gas temperature (0.1 K), gas temperature inhomogeneity (0.5%), gas pressure (0.05%) and frequency (1 MHz) to achieve this breakthrough error on X_{CH_4}.

Four studies based on Fourier transform spectroscopy (FTS) have investigated the R(6) manifold [23,24,25,26], all of them used a Voigt profile for the line shape analysis, except the work of Devi *et al*. [26] for which speed-dependence and line-mixing were included. More recently, high sensitivity cavity ring down spectroscopy (CRDS) measurements in support of the MERLIN mission were performed at NIST on the selected R(6) manifold at room temperature [27] and between 223 and 290 K [28]. Spectroscopic parameters of the six R(6) components were retrieved using the sophisticated Hartmann-Tran (HT) line profile [29,30] along with line-mixing effect [31] in the first order approximation [32]. In addition, the temperature dependence of the air-broadening, air-shifting and line-mixing parameters was derived. It was shown that the model was able to represent the measured data for large ranges of pressure and temperature conditions with a maximum relative residual of 0.4% (see Fig. 2 of [28]), the smallest obtained so far for this methane manifold. However, the setup used to measure the spectra at low temperature did not provide an accurate absolute frequency scale, but only an accurate relative frequency scale. This was taken into account in the analysis by introducing a global shift for each of the spectra [28]. However, this led to a potential source of error that does not meet the MERLIN prerequisites, and motivated the present work.

A new measurement campaign was thus conducted by CRDS at LIPhy-Grenoble, aiming to provide independent high quality spectra in order to accurately characterize the temperature dependence of the spectroscopic parameters for the six components contributing to the R(6) manifold. Particular attention was paid to the accurate determination of the frequency scale with the use of a comb-referenced cavity ring down spectrometer. Note that this setup was previously used for a CRDS study at room temperature of the water vapor lines interfering with the R(6) manifold in the 6071.4–6080.0 cm^{-1} spectral region [33], as atmospheric water vapor lines may bias the methane concentration retrieval.

In terms of line positions, the most accurate transition frequencies of the six components of the R(6) manifold of interest were determined by saturation spectroscopy. The recent Doppler free Lamb dip centers determined in [34] agree with the previous values of [35] within 5×10^{-7} cm^{-1} (15 kHz). These position values are valuable to be used as constraints in the line profile analysis of the pressure broadened and mostly unresolved R(6) manifold (see below).

Let us mention that very weak additional methane lines are present in the region of the strong R(6) $2\nu_3$ manifold. These weak lines were measured by differential absorption laser spectroscopy (DAS) at 296 K and 80 K using pure methane sample at low pressure [36,37,38]. The corresponding rovibrational assignments can be found in [39,40] for the $^{12}CH_4$ and $^{13}CH_4$ transitions, respectively. These parameters have been included in the last version of the GEISA database [41].

The characterization of the temperature dependence of absorption spectra by CRDS requires the challenging development of high finesse optical cavities regulated in temperature over the atmospheric temperature range. To our knowledge, up to now only two cavities of this type, described in [42] and [43], were built at NIST and at University of Science and Technology of China, Hefei, respectively. The former one was used a few years ago to measure the methane absorption spectra presented in [28]. At LIPhy, we developed a liquid nitrogen cooled cavity [44] to record spectra at 77 K but without the possibility of varying the temperature. Nevertheless, thanks to this know-how, we managed to develop a temperature-regulated high finesse cavity for this project. In fact, as described in the next paragraph, the development was performed in two steps: a prototype (hereafter called version V1) and an improved version (V2) fulfilling the requirements in terms of temperature uniformity were successively developed.

This paper is organized as follows: the used experimental setup and recorded spectra are described in Section 2 while the acquisition procedure is presented in Section 3. In Section 4, we detail the analysis using our in-house multi-spectrum fitting procedure, considering the HT profile along with line-mixing (first order approximation). The derived spectroscopic parameters and their

147 temperature dependences are presented together with comparisons between measurements and
148 calculations. Section 5 is devoted to the validation of the model and associated data with ground-
149 based TCCON atmospheric measurements. Some conclusions and perspectives close our report
150 (Section 6).

151 **2. Setup and spectra recordings**

152 The used comb-referenced cavity ring down spectrometer is similar to the one detailed in
153 [45,46] with two main differences: *(i)* the standard distributed feedback (DFB) laser diode is replaced
154 by a stabilized and narrowed laser diode [47] *(ii)* the room temperature CRDS cell is replaced by a
155 temperature regulated high finesse cavity (TR-HFC) as described in [48].

156 2.1. Optical feedback stabilized and narrowed DFB laser diode

157 The laser source is based on a DFB laser diode whose optical isolator has been removed. Part
158 of the emitted light is directed into a highly-stable V-shaped cavity [free spectra range (FSR) = 480
159 MHz; finesse= 500,000] made of ultra-low expansion glass. The optical feedback from this high-
160 finesse cavity is sent back into the DFB laser diode with the right phase allowing locking this latter to
161 one of the optical modes of the V-shaped cavity and narrowing its emission. The rest of the DFB laser
162 light passes through an optical isolator and a Mach-Zehnder modulator (MZM) driven by a
163 microwave signal generator (Model SMF 100A from Rohde & Schwartz). This modulator allows
164 generating a side band (the carrier being killed) which can be tuned between 1 GHz and 22 GHz
165 (corresponding to the frequency range of the signal generator) from the input frequency with an
166 efficiency of ~5%. As a result, a highly stable and narrow (sub-kHz) laser source is obtained which can
167 be tuned continuously over the entire DFB range (typically 25 cm^{-1}) by locking the laser diode to
168 different cavity modes and changing the side band frequency [49 and references herein].

2.2. The comb-referenced cavity-ring down spectrometer

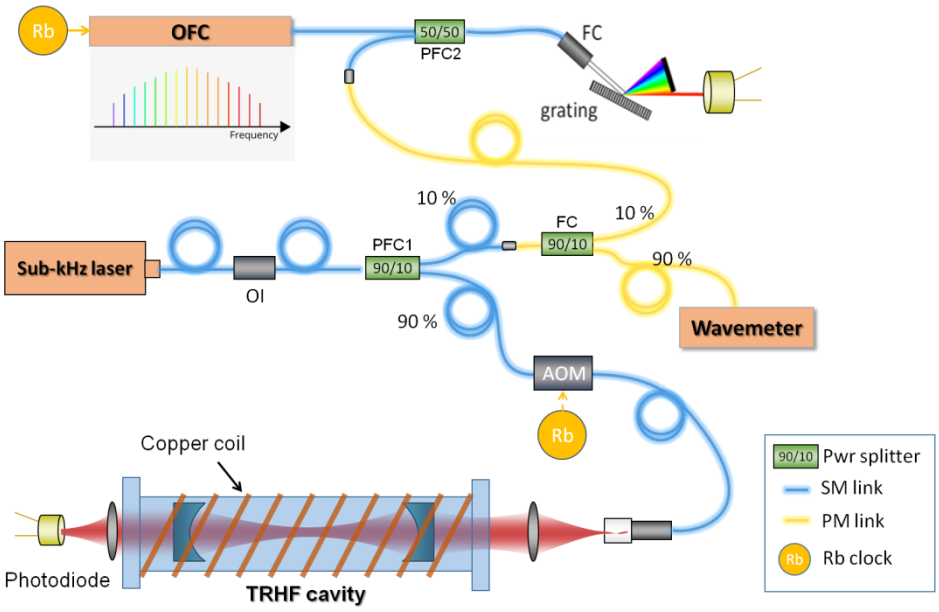

Figure 1. *Adapted from [50]. Scheme of the comb-referenced cavity ring down spectrometer with the temperature regulated high-finesse (TRHF) cavity. The different components include an optical isolator (OI), a fiber coupler (FC), two polarization-maintained fiber couplers (PFC1,2), an optical frequency comb (OFC), and acousto-optic modulator (AOM) referenced to a GPS referenced rubidium (Rb) clock.*

To achieve a sufficiently high optical power for CRDS recordings, the output beam is amplified by a boost optical amplifier (model BOA1082P from Thorlabs). Periodic resonances between the laser light and a CRDS cavity mode are obtained by applying a voltage triangular ramp on a PZT tube on which the output cavity mirror is mounted. The amplitude of the ramp corresponds to one FSR of the cavity. At each resonance, the transmitted light is detected by an InGaAs photodiode (model G8376-03 from Hamamatsu) and a ring down (RD) event is generated by switching-off the laser light with an acousto-optic modulator (AOM) (Model MT110-B14-IIR20 from AA Optronics) when the build-up signal on the detector is higher than a user-defined voltage threshold, V_{th}. The purely decreasing exponential signal of the RD is acquired with an ADC (16 bits; 1.25 MSpl/s) and fitted to derive the ring down time, τ, and the extinction coefficient, $\alpha(\nu)$, which corresponds to the difference between the loss rates for the cell filled with the gas mixture, $n/c\tau$ and evacuated, $1/c\tau_0$,

$$\alpha(\nu) = \frac{n}{c\tau(\nu)} - \frac{1}{c\tau_0(\nu)} \quad (1)$$

where c is the speed of light and n is the refractive index of the gas. $1/c\tau_0$ is related to the reflectivity of the mirrors, R, and the cavity length, L_{cav}:

$$\frac{1}{c\tau_0(\nu)} = \frac{1-R(\nu)}{L_{cav}} \quad (2)$$

In our experiment, with a cavity length of L_{cav}= 45 cm and the used high reflective mirrors (from Layertec, R>99.99%), the RD time, τ_0, is ~ 117 µs at 6077 cm^{-1}.

In order to increase the number of RD events per second, a tracking method is implemented here. This method consists in a RD tracking loop combined with a variable PZT waveform offset which leads to a reduction of the amplitude of the triangular ramp (see above) by a factor of about 100 and thus to a slower passage through resonance and a much better transmission of the cavity as discussed in [51]. This allows adopting a higher user-defined threshold thus reducing the noise level per ring-down.

For each RD event, the absolute frequency of the laser source is accurately determined thanks to a frequency comb (FC) (Model FC 1500-250 WG from Menlo Systems). More precisely, a part (~10%) of the light emitted by the laser source is superimposed to one output beam of the FC with a polarization maintaining fiber coupler. Thanks to a grating, only the light around the laser frequency is detected by a fiber-coupled auto-balanced InGaAs avalanche photodiode (model PDB570C from Thorlabs; DC-400 MHz bandwidth). A fast acquisition card (250 MHz-16 bits, by GAGE) allows digitizing the signal measured by the detector. After Fourier transform of this signal, the beat note frequency, f_{BN}, is determined using a peak determination procedure over the 0 to 125 MHz RF range at a 1 kHz repetition rate with a 7 kHz resolution. The absolute laser frequency, ν_{laser}, is deduced from the following equation:

$$\nu_{laser} = n_{mode} f_{rep} \pm f_{CEO} \pm f_{BN} + f_{AOM} \quad (3)$$

where f_{rep} and f_{CEO} are the repetition rate (= 250 MHz) and the carrier-envelop offset (here equal to -20 MHz) of the FC, respectively. These two frequencies are referenced to a GPS-referenced 10 MHz rubidium clock. The mode number, n_{mode}, to which the DFB laser diode is beating, is derived from the approximate laser frequency measured with a commercial Fizeau type wavemeter (HighFinesse WSU7-IR, 5 MHz resolution, 20 MHz accuracy over 10 h, 100 Hz refresh rate). The frequency of the sinusoidal wave, f_{AOM}, applied to the acousto-optic modulator, is delivered by a direct digital synthesizer (DDS). Both the fast ADC clock and DDS are referenced to the 10 MHz reference. Note that for convenience, two AOM are used (one implemented in the source, not used to switch off the light and the second one, just before the cavity as already mentioned). The total frequency shift due to these two AOM is exactly f_{AOM} = 210.1 MHz.

2.3. The temperature regulated high finesse cavities

Two versions (V1 and V2) of a temperature regulated high finesse cavity, working on the same principle as the one described in [48] were coupled to the above-described spectrometer. In both

versions, the cavity is placed inside a tube (702 mm long and 58 mm inner diameter). Compared to [48], new high reflectivity mirrors (from Layertec), suitable for the R(6) manifold near 6077 cm^{-1}, had to be mounted on the cell. They provide a reflection coefficient *R* larger than 99.99% over the 1500-1700 nm range. The main characteristics of the two cells are summarized in **Table 1.**

	Ext. tube	Thermal isolation	FSR (MHz)	Finesse[a]	Sensor	*ΔT* (K)	Temp. range (K)
V1	Stainless steel	Foam	258	~187,500	Pt1000 ⅓ DIN class B	<0.5	253…333
V2	Copper	Aerogel spaceloft® Gray SL10mm	332	~297,800	Pt100 1/10 DIN class B	<0.1	243…333

Table 1*. Main characteristics of the two temperatures regulated high finesse cavities used in this work.*

The V1 version of the temperature-regulated high finesse cavity, described in [48], was first used. Two counter-propagating copper coils, placed around the tube, allow for regulating the cell temperature thanks to a cooling fluid flowing through them. The fluid is either a low vapor pressure silicone oil for temperatures higher than room temperature (RT) or absolute ethanol for the lowest temperatures. The temperature of the fluid is regulated using a deported refrigerated/heating circulator (model Corio 1000F from Julabo). An inner copper tube is placed between the two mirrors to limit the convection and reduce exchange of the gas inside the tube with the surrounding gas so that the sounded gas can be considered as thermalized to the tube temperature (see below). This V1 cell was used for spectra recordings at 313, 303, 294, 283 and 273 K where temperature variations along the inner tube axis, *ΔT*, are kept below 0.3 K.

For the lowest temperatures, the temperature gradients, *ΔT,* obtained with the V1 cell were found too large (up to 0.5 K) and it was decided to develop a new version (V2) with reduced temperature gradients. The new cell is based on the same scheme but the outer stainless steel tube is replaced by a copper tube and the thermal isolation is improved thanks to the use of aerogel (spaceloft® Gray SL10mm). In addition, the four 3-wires 1000 Ω platinum temperature sensors (model P1K0.232.6W.Y.010 from Innovative Sensor Technology; ⅓ DIN class B ; accuracy: ±0.1 K to 0.2 K) installed on the inner copper tube of V1 are replaced by five 4-wires 100 Ω platinum temperature sensors (model P0K1.232.4W.K.010 from Innovative Sensor Technology; class 1/10 DIN) giving an accuracy equal to 0.03+0.0005*t* (with *t* the temperature in °C). The temperature sensors are measured and recorded with a high accuracy data logger (PT-104 from Pico technology; accuracy: 0.015 °C + 0.01% of reading). With this new cell, *ΔT* gradients smaller than 0.1 K are achieved over the entire temperature range of the measurements (243 to 333 K). We also ensured that the measured temperature is independent of the gas pressure in the cell. The temperature is also very

stable with time with observed variations of only 0.04 K over 14h at 253 K. This V2 cell was used for spectra recordings at 273, 263, 253 and 243 K.

To verify that the sounded gas is thermalized at the temperature of the inner copper tube *i.e.* that its temperature is identical to that measured by the sensors placed on the copper tube, we performed a series of measurements using 400 ppm of CO_2 in air as test species. Our goal was to determine the CO_2 rotational temperature from a series of $^{12}CO_2$ transitions and to compare it to the tube temperature. Recordings of the R(6) to R(20) lines of the 30013–00001 band at a measured temperature of 251.5 K were performed for total pressures of 750 and 250 Torr in the 6232-6243 cm^{-1} interval. For each transition, four sub-spectra were acquired following the procedure described in part 3.1. The Multi-spectrum Analysis Tool for Spectroscopy (MATS) from NIST [52] was used for the multi-spectra fit procedure with quadratic speed-dependent Nelkin-Ghatak profiles (qSDNGP) and the line-mixing effect (first-order approximation). For a given series of four sub-spectra, all the line profile parameters were fitted globally except the line intensity which was freed for each spectrum.

The temperature dependence of the line intensity, *S(T)*, is ruled by the Boltzmann factor:

$$S(T) = S(T_0)\frac{Q(T_0)}{Q(T)} exp\left[-c_2 E^{"}\left(\frac{1}{T}-\frac{1}{T_0}\right)\right] \quad (4)$$

where T_0 is a reference temperature (T_0= 296 K), c_2=1.4387769 cm K. *E"* is the lower state energy value and *Q(T)* is the internal partition function which were taken from the HITRAN database [53]. (The extremely weak stimulated emission term from the upper level of the transition is negligible). From accurately known intensity values at 296 K [54], S_{DLR}, the gas rotational temperature, *T*, can be obtained from:

$$ln\left[\left(S_{exp}(T_{cell})Q(T_{cell})\right)/\left(S_{DLR}(296K)Q(296K)\right)\right] = \left[\frac{1}{296}-\frac{1}{T}\right]c_2 E^{"} \quad (5)$$

The corresponding plot *versus E"* is presented in **Figure 2**. The gas temperature retrieved from the fitted slope (251.96±0.07 K) is in quasi-perfect agreement with the mean value of the four measured values of the copper tube temperature (251.98±0.04 K). We thus conclude that in our experimental conditions, the gas is at equilibrium and its temperature coincides with the measured temperature of the copper tube.

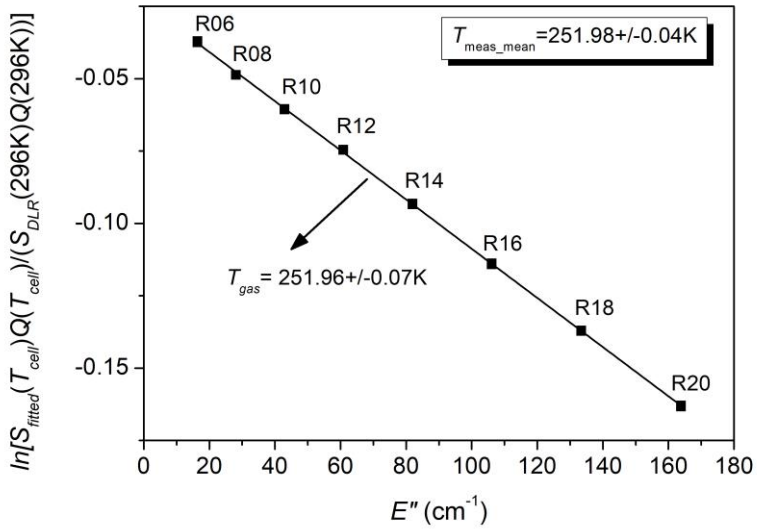

Figure 2. *Ratio of intensities retrieved in this work, from spectra recorded at 250 Torr and 252 K, over the ones measured with a 0.15% accuracy in [54] at 296 K (black squares). Ratios are weighted by the partition functions and their neperian logarithm is plotted versus E" for the R(6) - R(20) transitions of the 30013←00001 band of $^{12}CO_2$. The gas temperature retrieved from the fitted slope (251.96±0.07 K) shows a quasi-perfect agreement with the mean value of the temperatures provided by the four sensors placed on the copper tube (251.98±0.04 K).*

3. Spectra acquisition and obtained dataset

3.1. Acquisition procedure

About sixty spectra were recorded for temperature values between 243 and 313 K with a 10 K temperature step and total pressures between 50 and 750 Torr measured by a heated absolute capacitance manometer (Model AA02A Baratron from MKS; 1000 mbar full scale; accuracies derived from the certificate of calibration are respectively 0.04%, 0.05%, 0.05%, 0.07% and 0.10% for 750, 500, 250, 100 and 50 Torr). Each spectrum corresponds to the concatenation of four sub-spectra for the central part of the absorption line for all the pressures and two additional lower and upper wings sub-spectra for the recordings at 250, 500 and 750 Torr (**Figure 3**). A spectral sampling corresponding to the FSR of the cavity is adopted to increase the efficiency of the RD tracking loop (reducing the acquisition time) as the resonance always occurs at the same offset value of the ramp (see above). In order to provide more measurement points in the central part, four sub-spectra are recorded one at the starting frequency, f_{start}, and the others shifted from f_{start}, by ¼, ½ and ¾ of the FSR value. As a result, after concatenating these sub-spectra, the spectral resolution is improved by a factor of four.

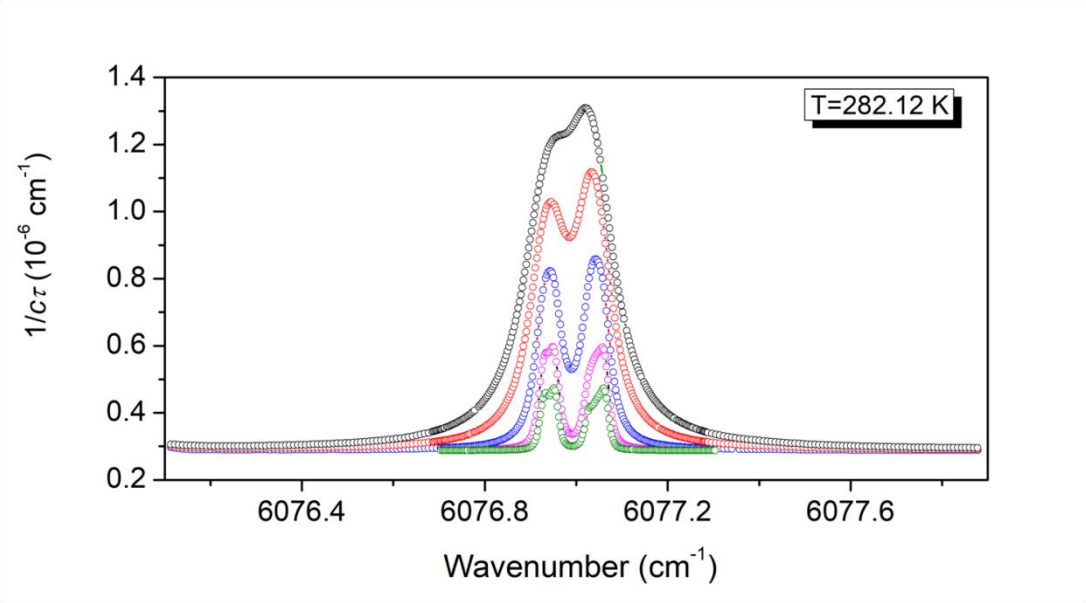

Figure 3. *Illustration of the spectral sampling applied to the spectra recorded at the different pressures (50, 100, 250, 500 and 750 Torr) at a temperature of ~282 K for a mixture with 2 ppm of CH_4.*

Increased absorption leads to shorter RD time and less photons reaching the detector. As a consequence, for a given number of RDs averaged per spectral point, the noise level at the top of the absorption line is greater than in the wings. To compensate this noise increase, an adaptative averaging procedure was implemented. In this way, the number of RD events averaged is automatically increased with the absorption until a user defined maximum value (in order to avoid too long acquisition times). Typically, 50 and 250 RD events were averaged in the wings and at the top of the absorption line, respectively.

3.2. Dataset

A total of 59 spectra was recorded for the different conditions of temperature and total pressure. For each temperature value, a series of spectra was recorded for total pressures equal to 750, 500, 250, 100 and 50 Torr (see **Figure 3**) and a gas mixture of CH_4 in air (Ar : ~1 Mol-%, O_2 : ~20.95 Mol-%, N_2 : ~78.05 Mol-%) with 1.984±0.03(2σ) Mol-ppm concentration. For the two lowest pressures (50 and 100 Torr), it was possible to increase the signal by using an additional mixture with a higher concentration of 8.022±0.08(2σ) Mol-ppm. The high signal-to-noise ratio (*S/N*) of the spectra is illustrated in **Figure 4** where two experimental spectra (one at 750 Torr and the other one at 50 Torr) are fitted independently with a quadratic speed-dependent Nelkin-Ghatak profile [29,30] and the line-mixing effect [31] for each of the six manifold components. The *Multi-spectrum Analysis Tool for Spectroscopy (MATS)* fitting program [52] developed at NIST was used for the fit. Note that the amplitude of etalon fringes was maintained below the noise level by tilting optical elements and using wedged windows for the temperature regulated cell and optical isolators. Residuals at the

noise level are achieved (lower panel of **Figure 4**), leading to quality factors (*QF*) of about 11 000 and 8000, respectively. (*QF* is defined as the ratio of the absorption at the peak to the *rms* of the residuals).

Note that each spectrum is accessible on Zenodo (DOI: 10.5281/zenodo.7325837) and corresponds to one file including the following columns: absolute wavenumber (in cm^{-1}), $1/c\tau$ (in 10^{-6} cm^{-1}), temperature (in °C) and total pressure (in Torr).

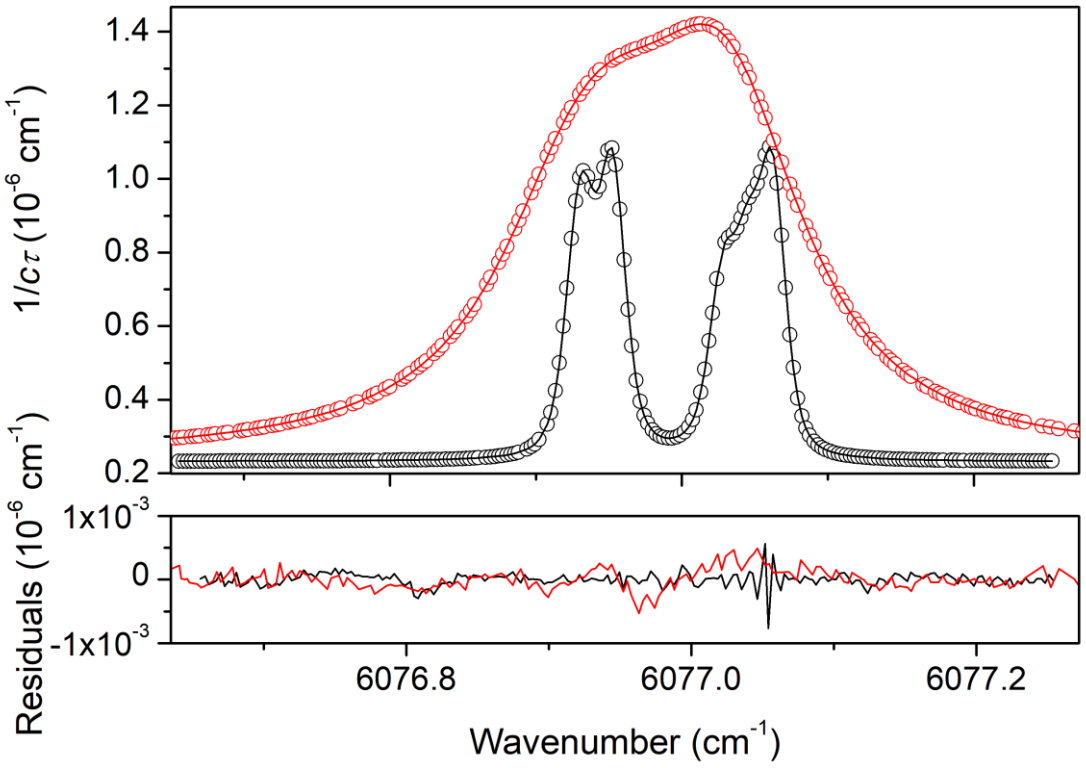

Figure 4. *Upper panel: R(6) manifold CRDS spectra recorded at 243 K and 750 Torr (red) and 253 K and 50 Torr (black) with mixtures of 2 ppm and 8 ppm of CH_4 in air, respectively.*
Lower panel: After subtraction of the simulated spectra (solid lines, upper panel), the obtained residuals are at the noise level, demonstrating high QF of about 11 000 and ~8000 for the spectrum at 750 Torr spectrum and 50 Torr, respectively.

3.3. Error budget of the recorded spectra and experimental temperature and pressure conditions

For each recorded spectrum, the temperature uncertainty is calculated from the square root of the quadratic sum of *(i)* the standard deviation of the temperature during the spectrum recording, *(ii)* the accuracy of the temperature sensors and *(iii)* the temperature gradient ΔT. Uncertainties between 0.16 and 0.28 °C are obtained for the V1 cell and between 0.05 and 0.07 °C for the V2 cell.

Pressure uncertainty of each spectrum corresponds to the square root of the quadratic sum of *(i)* the standard deviation of the pressure during the spectrum recording, *(ii)* the accuracy of the pressure gauge, which dominates. This leads to relative uncertainties of 0.04%, 0.05%, 0.05%, 0.07% and 0.10% for 750, 500, 250, 100 and 50 Torr, respectively. From the Allan variance of the BN frequency, the absolute frequency uncertainty of each spectral step (corresponding to the frequency averaged over 50 to 250 RD events) is estimated to be better than 10 kHz.

To evaluate the repeatability of our measurements, we considered two series of spectra recorded at 296 K 24 days apart and at 243 K two days apart. Spectra are then calculated for each series of spectra by fixing the temperatures and pressures to the measured ones and the spectroscopic parameters to their values reported in **Table 2**. Only the base line and the methane concentration were fitted for each spectrum. Comparison of residuals for the two series shows an almost perfect agreement at 296 K and 243 K and for all the pressures. The only exceptions are for the 750 and 500 Torr spectra at 296 K for which a maximum difference of 0.5‰ between the residuals is observed. We thus estimate the repeatability of the spectra to be negligible.

4. Fitting procedure and retrieval of the spectroscopic parameters and their temperature dependences

4.1. Spectra analysis and models

Following our analysis of the spectra of the R(6) manifold recorded at NIST [27,28], the present LIPhy spectra were analyzed using the multi-spectrum fitting code developed at LMD. First, we considered room temperature spectra (294 K): the 50 and 100 Torr spectra (8 Mol-ppm mixture) and the 250, 500 and 750 Torr spectra (2 Mol-ppm mixture) were fitted by simultaneous adjustment of the model parameters. Because the methane volume mixing ratio for all measured spectra does not exceed 8 ppm, we can safely neglect the methane self-broadening effects. The model used to analyze the room temperature spectra is the same as that of [27]. Specifically, the shape of the six R(6) lines at room temperature was modeled with the HT profile, with line-mixing effect taken into account through the first-order Rozenkranz approximation [32]. Within this approach, the absorption coefficient *versus* wavenumber σ (cm^{-1}) is calculated through [29]:

$$\alpha(\sigma) = \sum_l \frac{S_l n_{\mathrm{CH_4}}}{\pi}\left[\mathrm{Re}\left\{I_l^{HTP}(\sigma)\right\} - Y_l\,\mathrm{Im}\left\{I_l^{HTP}(\sigma)\right\}\right] + \sum_k \frac{S_k n_{\mathrm{CH_4}}}{\pi}\emptyset_k^{VP}(\sigma). \quad (6)$$

The first sum in Eq. (6) is over the six lines of the R(6) manifold, $Y_l = P\zeta_l$ being the first-order line-mixing parameter, S_l and $n_{\mathrm{CH_4}}$ the line-integrated intensity per number of density (at natural

isotopic abundance) and the number density of total methane, respectively. The second term corresponds to contributions of other weak interfering lines having intensities lower than 1.0×10^{-22} cm/molecule at temperature T = 296 K. The latter contributions were calculated using the Voigt profile (VP) and parameters from the GEISA2020 database [41] and then fixed. Note that we found that the use of GEISA2020 for these weak lines gave better results (lower residuals) than when using HITRAN2020 [53]. The main difference between the two databases in this region lies in the fact that GEISA2020 uses $^{12}CH_4$ line parameters from the WKLMC line list [38] whereas HITRAN2020 is based on $^{12}CH_4$ lines from GOSAT-2014 line list [55].

Within the HTP model, the $I_l^{HTP}(\sigma)$ line-shape quantity is a function of eight parameters [29], *i.e.*

$$I_{HTP}(\sigma) = f(\sigma - \sigma_0, \Gamma_D, \Gamma_0, \Gamma_2, \Delta_0, \Delta_2, \nu_{vc}, \eta), \quad (7)$$

with σ_0 representing the unperturbed position of the line, Γ_D the Doppler broadening, ν_{vc} the Dicke narrowing frequency and η the correlation parameter. The speed dependences of the collisional halfwidth $\Gamma(v)$ and shift $\Delta(v)$ are modeled by the quadratic law $\Gamma(v) + i\Delta(v) = \Gamma_0 + i\Delta_0 + (\Gamma_2 + i\Delta_2)[(v/\tilde{v})^2 - 3/2]$ [56,57]. ν_{vc}, Γ_0, Γ_2, Δ_0 and Δ_2 are proportional with the total pressure P while σ_0 and η are constant.

In our fitting procedure, for each of the six R(6) components, the shared parameters (*i.e.* common parameters for all considered pressures) are then $\frac{\Gamma_0}{P}, \frac{\Gamma_2}{P}, \frac{\Delta_0}{P}, \frac{\Delta_2}{P}, \frac{\nu_{vc}}{P}, \eta, \frac{Y}{P}$ together with the relative integrated line intensity, *i.e.* A_l/A_{tot} with $A_l = S_l n_{\mathrm{CH_4}}$ and A_{tot} the spectrum area. For all the lines, the zero-pressure position σ_0 was fixed to the highly accurate values (kHz uncertainty level) provided by Votava *et al.* [34]. For each spectrum, a linear baseline and the total spectrum area were also retrieved. The Doppler broadening is fixed to its theoretical value calculated at the measured temperature (using the NIST referenced molar mass of 16.0425 g.mol^{-1}). Since the concentrations of methane in the mixtures were not known with sufficient accuracy (*cf.* section 3.2), the absolute line intensities were determined from the relative intensities of the six R(6) lines retrieved in the multispectrum fits described here, and the sum of the intensities of these six lines given in HITRAN2020 [58] (*i.e.* S_{tot}= 5.17670x10^{21} cm/molecule).

Then, the temperature dependences of five line-shape parameters ($\Gamma_0, \Gamma_2, \Delta_0, \nu_{vc}, Y$) were derived using the spectra sets recorded at 312 K and 243 K. Note that in our previous study [28] the temperature dependences were deduced from the room temperature and the coldest spectra (*i.e.* 222 K). In this work, thanks to a better quality of the measured spectra, we were able to include both

the highest and the lowest temperatures spectra in the determination of the temperature dependences of the parameters.

The temperature dependences of the line-broadening Γ_0 and Γ_2, Dicke narrowing ν_{vc} and line-mixing Y_l coefficients are modeled by a power law, and that for the air-shifting Δ_0 by a linear function:

$$\Gamma(v,T) = \Gamma_0(T_0)\left(\frac{T_0}{T}\right)^{n_{\Gamma_0}} + \Gamma_2(T_0)\left(\frac{T_0}{T}\right)^{n_{\Gamma_2}}[(v/\tilde{v})^2 - 3/2], \quad (8)$$

$$i\Delta(v,T) = i\Delta_0(T_0) + \delta'(T - T_0) + i\Delta_2[(v/\tilde{v})^2 - 3/2], \quad (9)$$

$$Y_l(T) = Y_l(T_0)\left(\frac{T_0}{T}\right)^{n_Y}, \quad (10)$$

$$\nu_{vc}(T) = \nu_{vc}(T_0)\left(\frac{T_0}{T}\right)^{n_{vc}} \quad (11)$$

The other parameters (Δ_2 and η) were considered as temperature independent. In this fitting procedure, the room temperature parameters of the six R(6) lines were fixed to those obtained at 294 K, and only the temperature dependences described above were adjusted. In total 30 parameters describing the temperature dependence of the model were simultaneously adjusted along with a linear baseline and the total spectrum area of each spectrum. The relative intensities were fixed at the value determined at 294 K. The contributions of other weak interfering methane lines were calculated using the line parameters (and associated temperature dependence) provided by GEISA2020. Then, in a second step, the values of the obtained temperature dependences were used together with the room temperature model to perform direct comparisons with the spectra measured at other pressure and temperature conditions (see next section).

4.2. Fit residuals and obtained parameters

The results of the multi-spectrum fits at 312, 294, and 243 K, extending from 6076.7 to 6077.3 cm^{-1} are shown in **Figure 5** along with the residuals obtained from direct comparisons at other temperatures. **Figure 6** shows the maximum deviation at the ON line position between observed and calculated spectra obtained for all considered pressures and temperatures. The retrieved spectroscopic parameters are listed in **Table 2**.

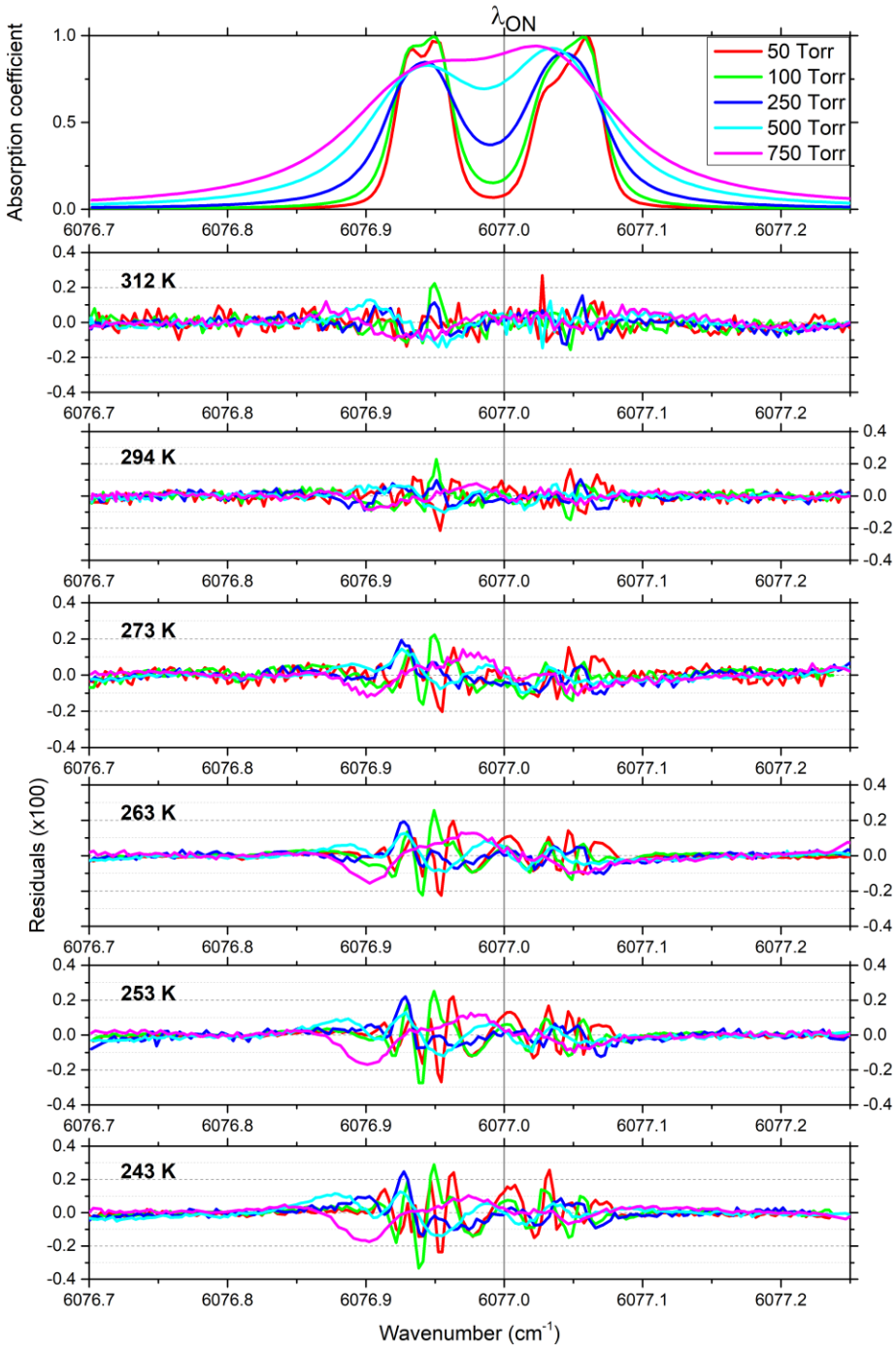

428

429 ***Figure 5.*** *'Obs.-Calc.' residuals between the CRDS spectra and our air-broadened temperature-dependent*
430 *spectroscopic model for the $2v_3$ R(6) $^{12}CH_4$ manifold. Only spectra measured at 312 K, 294 K and 243 K were*
431 *used in the multi-spectrum fits. Residuals for other temperatures are direct comparisons between the*
432 *measurements and the model. All the spectra were normalized to their peak absorption. The fit residuals are*
433 *multiplied by 100. The ON-line position of the MERLIN mission is indicated.*

434

435

436 **Table 2.** *Line parameters retrieved from the fit procedure for the R(6) manifold in the $2v_3$ band of $^{12}CH_4$ (given at*
437 *the reference temperature T_0=296 K).*

Parameter	R(6) transition					
	7E ← 6E 1	*7F1 ← 6F2 1*	*7A1 ← 6A2 1*	*7F1 ← 6F2 2*	*7F2 ← 6F1 1*	*7A2 ← 6A1 1*
σ_0 [a] *(cm^{-1})*	6076.927594 [a]	6076.934109 [a]	6076.953099 [a]	6077.027988 [a]	6077.046453 [a]	6077.062940 [a]
Intensity [b] *(cm/molecule)*	4.904(9)×10^{-22} [b]	7.544(15)×10^{-22} [b]	1.240(2)×10^{-22} [b]	7.415(15)×10^{-22} [b]	7.339(15)×10^{-22} [b]	1.217(2)×10^{-21} [b]
Γ_0 *(cm^{-1}/atm)*	0.06378(17)	0.055263(85)	0.063498(46)	0.055591(59)	0.043340(30)	0.059516(41)
n_{Γ_0}	0.6562(47)	0.5929(40)	0.7750(42)	0.7592(46)	0.7768(45)	0.7932(42)
Y_l *(cm^{-1}/atm)*	0	-0.3412(48)	-0.1611(27)	0.4297(38)	0.0977 (56)	0.0434(25)
n_Y	0	0.002(03)	2.072(30)	0.0002(02)	3.958(52)	2.640(84)
Γ_2 *(cm^{-1}/atm)*	0.01697(28)	0.00011(30)	0.01246(20)	0.00191(34)	0.00619(33)	0.00980(15)
n_{Γ_2}	1.257(18)	9.44(64)	0.762(19)	0.35(21)	0.073(58)	0.690(17)
Δ_0 *(cm^{-1}/atm)*	-0.02302(14)	-0.00524(08)	-0.01014(02)	-0.00673(03)	-0.01729(04)	-0.00795(02)
δ'*($10^{-5}cm^{-1}$/atm/K)*	12.4(2)	-2.3(1)	1.8(1)	1.7(1)	3.9(1)	3.0(1)
Δ_2 *(cm^{-1}/atm)*	-0.00494(13)	0.00746(22)	-0.00426(13)	-0.00432(71)	-0.00918(28)	0.001293(06)
ν_{vc} *(cm^{-1}/atm)*	0 [c]	0.0130(39)	0.0259(11)	0.0132(94)	0.0265(08)	0.0027(11)
n_{vc}	0	0 [c]	1.433(31)	0.476(85)	0 [c]	0.58(31)
η	0.171(27)	0.080(66)	0.363(17)	0.058(48)	0.775(26)	0 [c]

Notes

The uncertainties in parentheses are 1σ-errors in the last quoted digit(s). Note that the parameters presented in this table are truncated to accommodate the uncertainty values, however we recommend using the exact values reported in the supplementary material to avoid discrepancies with the fitted model.

[a] Fixed to values determined in [34].

[b] Absolute intensities given here are determined from relative intensities of the six R(6) lines retrieved in the multispectrum fits described in section 4, and the sum of the six line intensities given in HITRAN2020 [58] (S_{tot}= 5.17670×10^{-21} cm/molecule).

[c] Ill-defined parameter, set to 0.

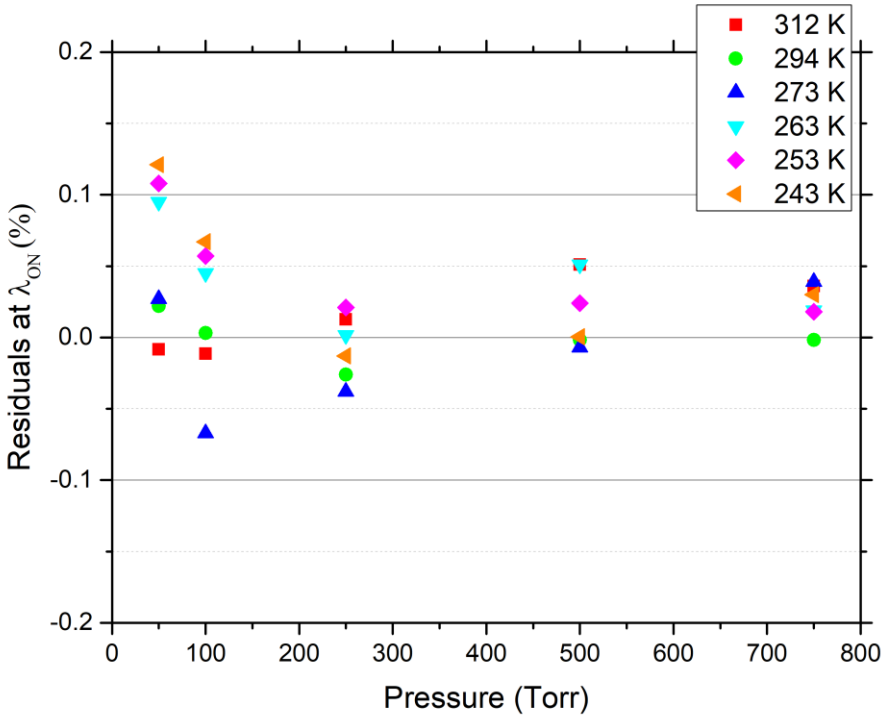

Figure 6. *Deviations between observed and calculated spectra obtained for all considered pressure and temperature conditions at the ON line position of MERLIN.*

Considering first the room temperature model (residuals and λ_{ON} deviations at 294 K, **Figures 5 and 6**, respectively), an excellent agreement is obtained with a maximum residual deviation of 0.2% for all considered pressures, and an ON-line deviation lower than ±0.03%. Compared to our previous model [27], the agreement at the ON-line position is improved by more than a factor of 3 (±0.03% compared to ±0.1%). Further exploration of the MERLIN error budget, considering the spectroscopic model reported here, is planned in a future work.

Now considering the residuals for other temperature conditions, it appears that although a good agreement is found between the measured and fitted/calculated spectra, the deviation between these two increases as the temperature decreases. Indeed, the maximum deviation is only 0.2% at 312 K and 273 K, but is around 0.3% at 243 K. The same observation can be done for the ON-line deviation, which is however always lower than 0.1% (except for the lowest pressure spectra at 243 K and 253 K for which the deviation reaches 0.12%). Again, these results must be compared with our previous model [28], for which maximum deviations reach 0.4% for low temperatures (242 K and 272 K). Apart from the fact that our new model is in better agreement with the measured spectra, it must be highlighted that the absence of jitter of the laser frequency and the very accurate absolute

frequency scale in these new measurements is believed to make our new spectroscopic model more robust.

The obtained room temperature line shape parameters (**Table 2**) are significantly different from those determined in Delahaye *et al.* (*cf.* Table 2 of [27]). Specifically, differences up to several percent's are observed for the line broadening coefficients and even more for refined line shape parameters. Similar observations are obtained for the temperature dependences (*cf.* Table 2 of [28]). In fact, because of the strong overlapping between the R(6) lines within the considered temperature and pressure conditions and the large number of parameters to be retrieved, significant correlations between the parameters cannot be avoided and the fitted parameters have to be considered as mostly effective. Moreover, here we fixed the line positions of the R(6) transitions to those of Votava [34] while they were adjusted in Ref. [27]. For these reasons, it is not meaningful to directly compare the sets of parameters from these different studies. However, direct comparisons (not shown here) between the measured spectra of Refs. [27] and [28] and those simulated using the present set of parameters led to quantitatively similar residuals as those obtained with the old parameter set, shown in Refs.[27] and [28]. As a consequence, the parameters listed in **Table 2** are self-consistent and must always be used together. They provide the best available modeling of the absorption in the R(6) manifold of the $2\nu_3$ band of $^{12}CH_4$ over large pressure and temperature ranges.

A complete line list of the CH_4 lines considered in the fitting procedure (between 6076 and 6078 cm^{-1}) is provided as a supplementary material. The R(6) parameters are those determined in this work and reported in **Table 2**. Please note that the parameters presented in this table are truncated to accommodate the uncertainty values, however we recommend using the exact values reported in the supplementary material in order to avoid any discrepancies with the fitted model. The parameters of other weak lines in the region, along with self-broadening and shifting coefficients of the R(6) lines, not determined here, are taken from GEISA2020.

4.3 Estimated error budget on the spectroscopic parameters

The uncertainties on the spectroscopic parameters retrieved from the multi-spectrum fit procedure contain two contributions. The first one is the statistical uncertainty (A-type uncertainty) which depends on the experimental noises. This contribution is computed directly in our fitting code. The second contribution is due to uncertainties on the measured temperature and pressure (B-type uncertainty). In order to evaluate this contribution, the following procedure was adopted. For the room temperature case, we first generated a set of spectra at the five pressures of the recordings using the spectroscopic parameters reported in **Table 2**. We then perturbed the total pressure or the temperature using the maximum uncertainty for each pressure or for the temperature, as detailed in

Sec. 3.1. Then we fit the simulated spectra with the "true" pressures or temperature. The retrieved spectroscopic parameters, using the multi-spectrum fit procedure, are then compared to the values used to generate the spectra. The B-type uncertainty was therefore obtained for room temperature spectroscopic parameters. The same procedure was then applied to the spectra used in the determination of the temperature dependences on the line shape parameters. The final uncertainty was then computed as the square root of the quadratic sum of the A-type and B-type uncertainties and reported in **Table 2**.

5. Validation tests with ground-based atmospheric measurements

The spectroscopic model and corresponding line parameters derived from the experimental spectra were then used to simulate atmospheric measurements. Fifty ground-based solar absorption spectra, measured at different zenith angles spanning from 23° to 82° and for various water vapor concentrations were selected for this validation test. These spectra were recorded at the TCCON facility in Park Falls, Wisconsin, between 2014 and 2017. The 6075-6078 cm^{-1} spectral range was considered for the comparisons. Calculations were made using the SPARTE calibration/validation chain developed at LMD, and widely described in [59]. The temperature and pressure profiles, taken from the NCEP database, were divided in 71 layers. The temperature, pressure and gas volume mixing ratio were linearly interpolated in each layer. Absorptions by CH_4, H_2O and CO_2 were considered in the calculation, standard atmospheric profiles being used as *a priori* profiles. Contributions of CO_2 and CH_4 weak lines were calculated using spectroscopic data provided by the last version of the GEISA database [41]. Note that for H_2O, the line parameters determined in [33] using a speed dependent Nelkin-Ghatak profile were used in place of GEISA2020. For the six lines of the $2v_3$ R(6) manifold, three calculations were performed: in the first one the present spectroscopic data and model were used (green), whereas in the second and third calculations we used data from our previous work [28] (blue) and from the GEISA2020 database [41] (red). Note that in the last case, the Voigt profile was used to model the absorption lines. For each molecular species, a scaling factor applied to the *a priori* profiles was retrieved. A linear baseline for the 100% transmission and a frequency calibration were also adjusted for each considered spectrum. Finally, the simulated spectrum was convolved with the apparatus line-shape function, provided by the TCCON station.

Figure 7 shows the comparisons between the simulated and measured TCCON spectra. For visualization purpose, on the upper panel, we present the TCCON spectrum averaged over the 50 spectra (thus corresponding to different recording and atmospheric conditions). The 'Calc.–Obs.' residuals obtained for each of the fifty spectra were averaged and are plotted on the middle panel. Finally, on the lower panel, we present the associated standard deviations of the 'Calc.–Obs.' deviations. As described in [57], averaging the 'Calc.–Obs.' differences helps to decrease the

524 measurement noise (at least its random part), and to reveal systematic errors that can be mainly
525 attributed to the spectroscopic model. No obvious feature remains in the residuals obtained with our
526 present model except for a weak feature around 6077.2 cm^{-1}. The analyses of the 'Calc.–Obs.'
527 standard deviations of the fifty individual spectra (lower panel) help us determining if the
528 measurement conditions (solar zenith angle, season, humidity) have an impact on the bias (the lower
529 the standard deviation is, the less condition-dependent the model is). We note that the above-
530 mentioned 'Calc.–Obs.' feature at 6077.2 cm^{-1} is spectrum independent as it is not observed on the
531 lower panel. This structure might be related to a solar line located near this position. On the
532 opposite, the plot of the standard deviations shows a clear structure near 6075.5 cm^{-1}, which is both
533 due to a water line and a solar line, but has no impact at the OFF- and ON- line positions of the
534 MERLIN mission.

535 As a comparison, **Figure 8** shows differences between two simulated and measured TCCON
536 spectra (no average) for two different solar zenith angle (29° and 65°) the same day (07/05/2017). As
537 can be observed, the present spectroscopic model leads to the best agreement with the
538 measurements, residuals being within the TCCON measurement noises, while larger differences are
539 obtained with the Voigt profile from GEISA2020, and, to a lesser extent, with the model from our
540 previous studies [27,28]. It is worth pointing out that our new model succeeds in significantly
541 decreasing the amplitude of the residuals while keeping the standard deviation to a very low level.
542 Particularly, the ON-line region exhibits flat residuals and standard deviations. These results obtained
543 over a significant number of atmospheric situations illustrate the improvements achieved with the
544 developed model in atmospheric spectra calculations. Further analyses of atmospheric observations
545 are planned, in which the retrieved methane volume-mixing ratio will be validated with reference
546 measurements.

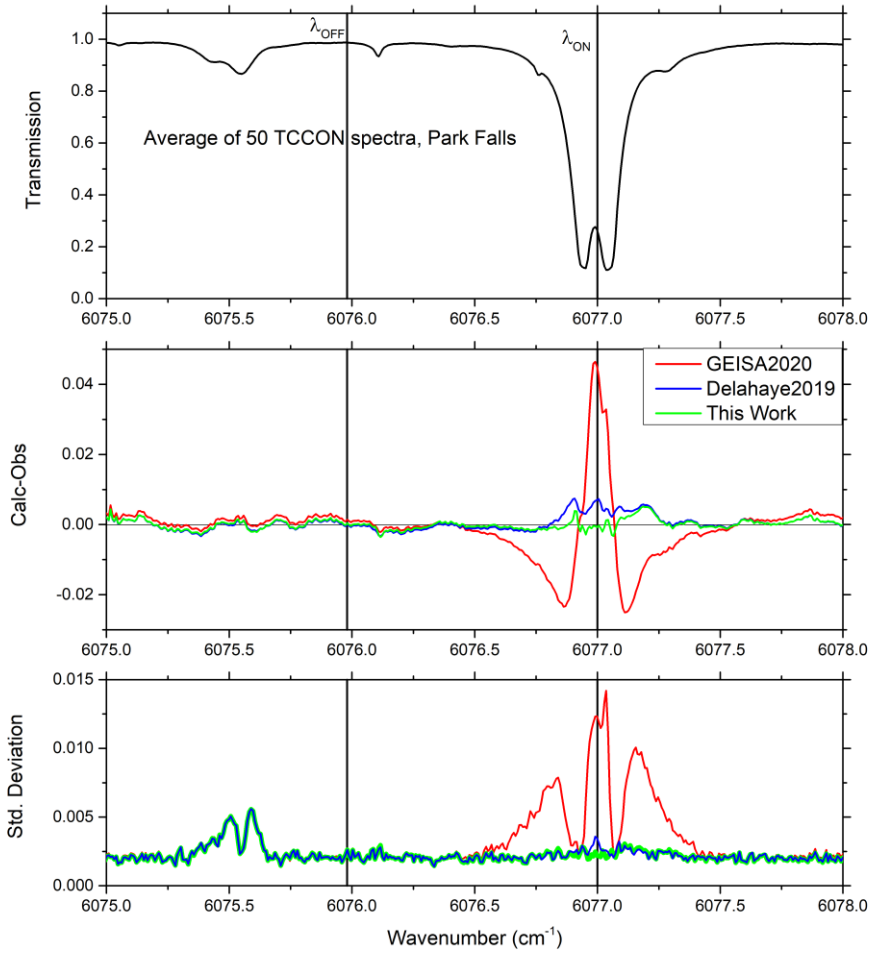

Figure 7*. (Top) Ground-based transmission spectrum averaged over 50 spectra measured by Fourier transform spectrometer at Park Falls facility in the MERLIN spectral region. (Middle) Residuals obtained from simulations of these measurements using methane spectroscopic data and model of the present work, along with those obtained using data from [28] (*i.e. *Delahaye2019) and the 2020 version of GEISA. (Bottom) The corresponding standard deviations. The ON-and OFF-line positions of the MERLIN mission are indicated.*

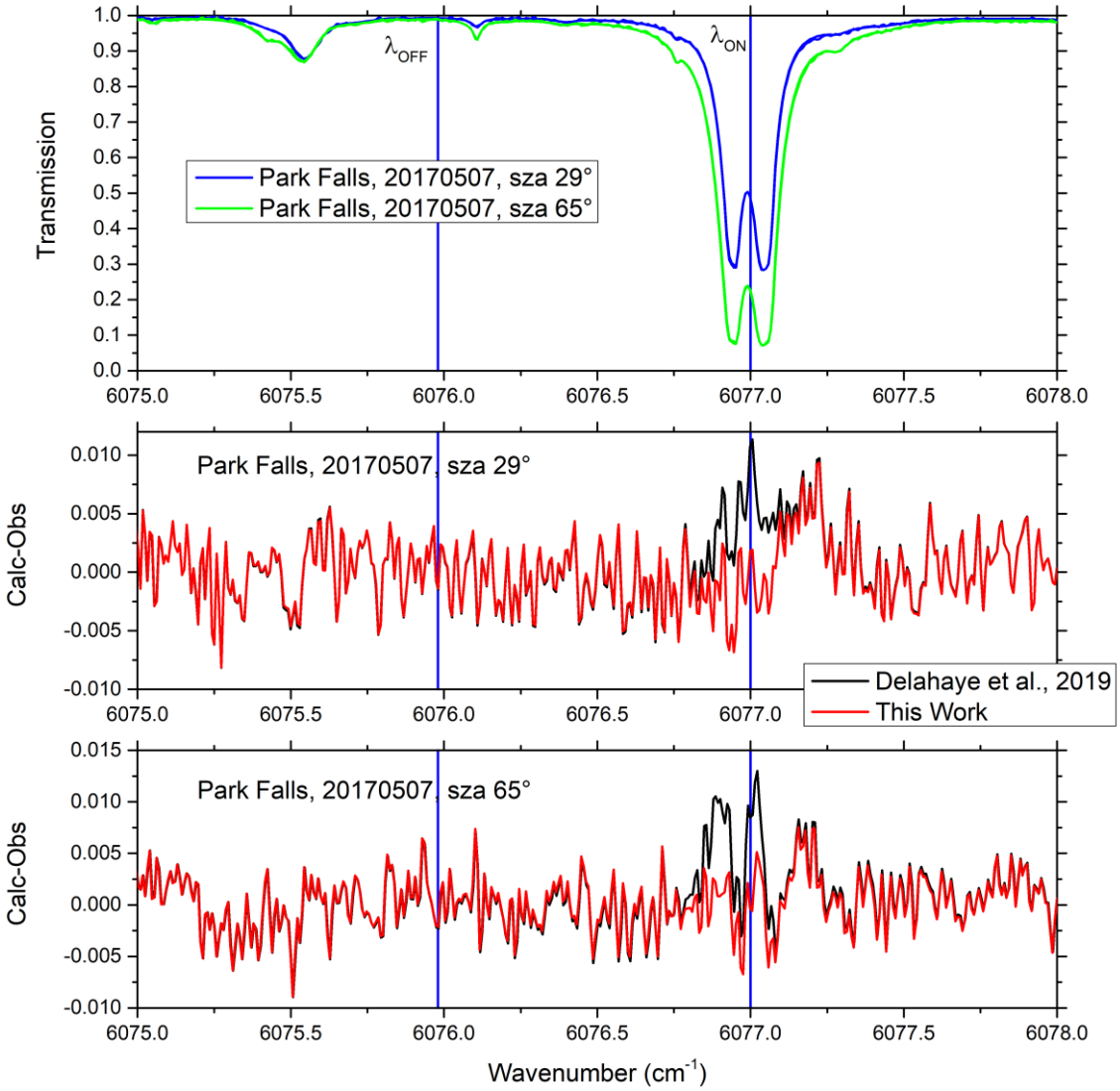

Figure 8. *(Top) Ground-based transmission spectra measured by Fourier transform spectrometer at Park Falls for two solar zenith angles (SZAs) in the MERLIN spectral region. Residuals obtained from simulations of these measurements using methane spectroscopic data from the present work and [28] (i.e. Delahaye2019) are plotted in the middle and bottom panels. The ON-and OFF-line positions of the MERLIN mission are indicated.*

6. Conclusion

Precise modelling of methane absorption cross-section in the 1.64-µm region for atmospheric temperature and pressure conditions is needed to meet the accuracy requirement of the MERLIN. In previous studies [27,28], using high-quality laboratory measurements from NIST and the most advanced line shape model, we deduced a set of spectroscopic parameters capable of representing the measured cross sections over a wide temperature and pressure range with a maximum relative residual of 0.4%. However, the lack of an accurate absolute frequency scale limited their robustness.

In the present work, absorption of methane in the 1.64 µm region was accurately measured using a comb-referenced cavity ring-down spectrometer with a high finesse cavity temperature regulated between 243 K and 313 K. A particular attention was paid to the absolute frequency scale

calibration and temperature stability of the cell. The spectra recorded in different temperature and pressure conditions were analysed using the latest standard line shape profile which considers line-mixing, Dicke narrowing and speed dependence effects. The obtained data and model enable calculation of synthetic spectra to within 0.1% of measurements at the ON-line MERLIN position of the MERLIN mission. It is nevertheless worth underlying that the differences between the values of the room temperature line shape parameters derived in this work and those derived from the NIST spectra [27], largely exceeds their statistical uncertainties provided by the fit. This is also the case for the temperature dependence parameters obtained in this work and in Ref. [28]. This matter of fact is only partly due to the different experimental datasets. The set of parameters provided as Supplementary Material allows for a satisfactory reproduction of the R(6) MERLIN manifold in atmospheric conditions but the parameter values should be considered as effective values. The considerable line overlapping of the considered R(6) manifold leads to considerable correlations between the model parameters and the absolute parameter values should be used with caution.

Comparisons between the present new model and ground-based atmospheric measurement were made and show significant improvement with respect to existing spectroscopic models of methane absorption in this spectral region. The present results can be readily applied not only to the MERLIN spectra but also to the methane Earth atmospheric remote sensing in general (*e.g.* TCCON, Greenhouse Gases Observing Satellite, and Network for the Detection of Atmospheric Composition Change). In the frame of the MERLIN mission remaining open issues are:

- The measurement of spectral shape parameters of methane lines broadened by water vapour and the determination of their impact on the absorption cross-sections at λ_{ON},
- The modification of Level 2 by using *P,T*-interpolated residual absorption cross-sections (the systematic residuals being mostly due to line model deficiency) to achieve the requirements,
- If necessary, an improved handling of line-mixing effects by replacing the fit of the first-order ζ parameter by that of the real part of the off-diagonal elements of the relaxation matrix to have a less effective and more physical modelling of the manifold [31].

Acknowledgements

CNES is acknowledged for the support of S. Vasilchenko for eight months at LIPhy. This work was partly funded by the European Space Agency (ESA) through the contract No. 4000132228/20/I-NS with Deutsches Zentrum fuer Luft- und Raumfahrt) entitled Improved Spectroscopy for Carbon Dioxide, Oxygen, and Water Vapour Satellite Measurements for which the authors are sub-contractants. M. Birk and G. Wagner (DLR) are acknowledged for their continuous support and for

fruitful discussions in particular about improvements of the developed CRDS cell and the spectra analysis. E. M. Adkins and D. A. Long from NIST are also greatly thanked for their contribution to the comparison/validation of the multi-spectrum fit program used in this work to the MATS program. The ANR projects e_PYTHEAS (ANR-16-CE31-0 0 05) and TEMMEX (ANR-21-CE30-0053-01) partly supported this work.

607 **References**

[1] Ciais P, Sabine C, Bala G, Bopp L, Brovkin V, Canadell J, et al. Carbon and other biogeochemical cycles. In T. F. Stocker, *et al.* (Eds.), Climate change 2013: The physical science basis. Contribution of Working Group I to the Fifth Assessment Report of the Intergovernmental Panel on Climate Change (Chap. 6, pp. 465–570). Cambridge, UK and New York: Cambridge University Press. (2013)

[2] Kirschke S, Bousquet P, Ciais P, Saunois M, Canadell J G, Dlugokencky E J, *et al.* Three decades of global methane sources and sinks. Nature Geoscience, 2013;6:813–823. Doi: 10.1038/ngeo1955

[3] Nisbet E G, Dlugokencky E J, & Bousquet P. Methane on the rise—Again. Science 2014;343 :493–495. Doi: 10.1126/science.1247828

[4] Nisbet E G, Dlugokencky E J, Manning M R, Lowry D, Fisher R E, France J L, *et al*. Rising atmospheric methane: 2007–2014 growth and isotopic shift. Global Biogeochemical Cycles 2016;30 :1356–1370. Doi: 10.1002/2016gb005406

[5] Saunois M, Bousquet P, Poulter B, Peregon A, Ciais P, Canadell J G, *et al.* Variability and quasi-decadal changes in the methane budget over the period 2000–2012. Atmospheric Chemistry and Physics 2017;17:11,135–11,161. Doi: 10.5194/acp-17-11135-2017

[6] Schaefer H, Fletcher S E M, Veidt C, Lassey K R, Brailsford G W, Bromley T M, *et al.* A 21st century shift from fossil-fuel to biogenic methane emissions indicated by $^{13}CH_4$. Science 2016;352:80–84. Doi: 10.1126/science.aad2705

[7] Prather M J, Holmes C D, Hsu J. Reactive greenhouse gas scenarios: Systematic exploration of uncertainties and the role of atmospheric chemistry. Geophys Res Lett 2012;39:L09803. Doi: 10.1029/2012GL051440

[8] Frankenberg C, Aben I, Bergamaschi P, Dlugokenckv E J, van Hees R, Houweling S, *et al.* Global column averaged methane mixing ratios from 2003 to 2009 as derived from SCIAMACHY: Trends and variability. J of Geophys Res 2011;116:D04302. Doi: 10.1029/2010JD014849

[9] Parker R, Boesch H, Cogan A, Fraser A, Feng L, Palmer P I, *et al*. Methane observations from the Greenhouse Gases Observing SATellite: Comparison to ground-based TCCON data and model calculations. Geophys Res Lett 2011;38:L15807. Doi: 10.1029/2011GL047871

[10] Buchwitz M, Reuter M, Bovensmann H, Pillai D, Heymann J, Schneising O, *et al*. Carbon monitoring satellite (CarbonSat): Assessment of atmospheric CO_2 and CH_4 retrieval errors by error parameterization. Atmospheric Measurement Techniques 2013;6:3477–3500. Doi: 10.5194/amt-6-3477-2013

[11] Butz A, Galli A, Hasekamp O, Landgraf J, Tol P, Aben I. TROPOMI aboard Sentinel-5 Precursor: Prospective performance of CH_4 retrievals for aerosol and cirrus loaded atmospheres. Remote Sensing of Environment 2012;120:267–276. Doi: 10.1016/j.rse.2011.05.030

[12] Chalon G, Cayla F, Diebel D. IASI: An Advanced Sounder for Operational Meteorology. Proceedings of the 52nd Congress of IAF, Toulouse France, October 2001, 2001.

[13] Crevoisier C, Nobileau D, Fiore A M, Armante R, Chedin A, Scott N A. Tropospheric methane in the tropics—First year from IASI hyperspectral infrared observations. Atmospheric Chemistry and Physics, 2009;9:6337–6350. Doi: 10.5194/acp-9-6337-2009

[14] Cressot C, Chevallier F, Bousquet P, Crevoisier C, Dlugokencky E J, Fortems-Cheiney A, *et al*. On the consistency between global and regional methane emissions inferred from SCIAMACHY, TANSO-FTS, IASI and surface measurements. Atmospheric Chemistry and Physics 2014;14:577–592. Doi: 10.5194/acp-14-577-2014

[15] Jacob D J, Turner A J, Maasakkers J D, Sheng J, Sun K, Liu X, *et al*. Satellite observations of atmospheric methane and their value for quantifying methane emissions. Atmospheric Chemistry and Physics 2016;16:14,371–14,396. Doi: 10.5194/acp-16-14371-2016

[16] Ehret G, Bousquet P, Pierangelo C, Alpers M, Millet B, Abshire J, *et al*. MERLIN: A French-German space lidar mission dedicated to atmospheric methane. Remote Sensing 2017;9. Doi: 10.3390/rs9101052

[17] https://atmos.eoc.dlr.de/isogg/about/

[18] Morino I, Uchino O, Inoue M, Yoshida Y, Yokota T, Wennberg P O, *et al*. Preliminary validation of column-averaged volume mixing ratios of carbon dioxide and methane retrieved from GOSAT short-wavelength infrared spectra. Atmospheric Measurement Techniques 2011;4:1061–1076. Doi: 10.5194/amt-4-1061-2011

[19] Kiemle C, Quatrevalet M, Ehret G, Amediek A, Fix A, Wirth M. Sensitivity studies for a space-based methane lidar mission. Atmospheric Measurement Techniques 2011;4:2195–2211. Doi: 10.5194/amt-4-2195-2011

[20] Kiemle C, Kawa S R, Quatrevalet M, Browell E V. Performance simulations for a spaceborne methane lidar mission. J Geophys Res: Atmospheres 2014;119:4365–4379. Doi: 10.1002/2013JD021253

[21] Pierangelo C, Millet B, Esteve F, Alpers M, Ehret G, Flamant P H, *et al*. MERLIN (Methane Remote Sensing Lidar Mission): An overview, Paper presented at 27th International Laser Radar Conference, EPJ Web of Conferences, New York, July 5–10, 2015.
[22] Stephan C, Alpers M, Millet B, Ehret G, Flamant P, Daniel C. MERLIN: A space-based methane monitor. In Proc. SPIE 8159, Lidar Remote Sensing for Environmental Monitoring XII, 2011
[23] Frankenberg C, Warneke T, Butz A, Aben I, Hase F, Spietz P, Brown L R. Pressure broadening in the $2\nu_3$ band of methane and its implication on atmospheric retrievals. Atmospheric Chemistry and Physics 2008;8:10,021–10,055. Doi: 10.5194/acpd-8-10021-2008
[24] Lyulin O M, A V Nikitin V I, Perevalov, I Morino, T Yokota, R Kumazawa, T Watanabe. Measurements of N_2- and O_2-broadening and shifting parameters of methane spectral lines in the 5550–6236 cm^{-1} region J Quant Spectrosc Radiat Transfer 2009;110:654–668. Doi : 10.1016/j.jqsrt.2009.02.012
[25] Lyulin O M, V I Perevalov, I Morino, T Yokota, R Kumazawa, T Watanabe. Measurement of self-broadening and self-pressure induced shift parameters of the methane spectral lines in the 5556–6166 cm^{-1} range J Quant Spectrosc Radiat Transfer 2011;112:531–539. Doi : 10.1016/j.jqsrt.2010.10.010
[26] Devi V M, Benner D C, Sung K, Crawford T J, Yu S, Brown L R, *et al*. Self- and air-broadened line shapes in the $2\nu_3$ P and R branches of $^{12}CH_4$. J Molec Spectrosc 2015;315:114–136. Doi: 10.1016/j.jms.2015.05.003
[27] Delahaye T, Maxwell SE, Reed ZD, Lin H, Hodges JT, Sung K, Devi VM, Warneke T, Spietz P, Tran H. Precise methane absorption measurements in the 1.64 µm spectral region for the MERLIN mission. J Geophys Res Atmos 2016;121:7360–7370. Doi: 10.1002/ 2016JD025024.
[28] Delahaye T, Ghysels M, Hodges JT, Sung K, Armante R, Tran H. Measurement and modeling of air-broadened methane absorption in the MERLIN spectral region at low temperatures. J Geophys Res Atmos 2019;124:3556–3564. Doi : 10.1029/2018JD028917.
[29] Ngo N H, Lisak D, Tran H, Hartmann J-M. An isolated line-shape model to go beyond the Voigt profile in spectroscopic databases and radiative transfer codes. J Quant Spectrosc Radiat Transf 2013;129:89–100. Doi: 10.1016/j.jqsrt.2013.05.034
[30] Tennyson J, Bernath P F, Campargue A, Császár A G, Daumont L, Gamache R R, *et al*. Recommended isolated-line profile for representing high-resolution spectroscopic transitions (IUPAC technical report). Pure and Applied Chemistry 2014;86:1931–1943. Doi: 10.1515/pac-2014-0208
[31] Hartmann J-M, Boulet C, Robert D, Chapter IV - Collisional line mixing (within clusters of lines), Editor(s): J-M Hartmann, C Boulet, D Robert, Collisional Effects on Molecular Spectra (Second Edition), Elsevier, 2021, Pages 181-289. Doi : 10.1016/B978-0-12-822364-2.00004-0.
[32] Rosenkranz PK. Shape of the 5 µm oxygen band in the atmosphere. IEEE Trans Antennas Propag 1975;23:498–506.
[33] Vasilchenko S, Tran H, Mondelain D, Kassi S, Campargue A. Accurate absorption spectroscopy of water vapor near 1.64 µm in support of the MEthane Remote LIdar missioN (MERLIN). J Quant Spectrosc Radiat Transf 2019;235:332-342. Doi : 10.1016/j.jqsrt.2019.06.027.
[34] Votava O, Kassi S, Campargue A, Romanini D Comb coherence-transfer as a widely tunable laser source for cavity ring down saturation metrology: kHz-accurate transition frequencies in the $2\nu_3$ methane band around 1.64 µm. Phys Chem Chem Phys 2022;24:4157–4173. Doi: 10.1039/d1cp04989e
[35] Gotti R, Prevedelli M, Kassi S, Marangoni M, Romanini D. Feed-forward coherent link from a comb to a diode laser: application to widely tunable cavity ring-down spectroscopy. J Chem Phys 2018;148:054202. Doi: 10.1063/1. 5018611.
[36] Gao B, Kassi S, Campargue A. Empirical low energy values for methane transitions in the 5852-6181 cm^{-1} region by absorption spectroscopy at 81 K. J Mol Spectrosc 2009;253:55–63. Doi: 10.1016/j.jms.2008.09.005.
[37] Wang L, Kassi S, Campargue A. Temperature dependence of the absorption spectrum of CH_4 in the region of the $2\nu_3$ band at 1.66 µm by absorption spectroscopy at 81 K. J Quant Spectrosc Radiat Transfer 2010;111:1130-1140. Doi: 10.1016/j.jqsrt.2009.10.019.
[38] Campargue A, Leshchishina O, Mondelain D, Kassi S, Coustenis A. An improved empirical line list for methane in the region of the $2\nu_3$ band at 1.66 µm. J Quant Spectrosc Radiat Transfer 2013;118:49-59. Doi: 10.1016/j.jqsrt.2012.12.004
[39] Nikitin AV, Chizhmakova IS, Rey M, Tashkun SA, Kassi S, Mondelain D, Campargue A, Tyuterev Vl G. Analysis of the absorption spectrum of $^{12}CH_4$ in the region 5855–6250 cm^{-1} of the $2\nu_3$ band. J Quant Spectrosc Radiat Transfer 2017;203:341-348. Doi : 10.1016/j.jqsrt.2017.05.014.
[40] Starikova E, Nikitin AV, Rey M, Tashkun SA, Mondelain D, Kassi S, Campargue A, Tyuterev Vl G. Assignment and modelling of the absorption spectrum of $^{13}CH_4$ at 80 K in the region of the $2\nu_3$ band (5853-6201 cm^{-1}) J Quant Spectrosc Radiat Transfer 2016;177:170–180. Doi:10.1016/j.jqsrt.2015.12.023.

[41] Delahaye T, Armante R, Scott NA, Jacquinet-Husson N, Chédin A, Crépeau L, Crevoisier C, Douet V, Perrin A, Barbe A, Boudon V, Campargue A, Coudert LH, Ebert V, Flaud J-M, Gamache RR, Jacquemart D, Jolly A, Kwabia Tchana F, Kyuberis A, Li G, Lyulin OM, Manceron L, Mikhailenko S, Moazzen-Ahmadi N, Müller HSP, Naumenko OV, Nikitin A, Perevalov VI, Richard C, Starikova E, Tashkun SA, Tyuterev Vl G, Vander Auwera J, Vispoel B, Yachmenev A, Yurchenko S. The 2020 edition of the GEISA spectroscopic database. J Molec Spectrosc 2021; 380:111510. Doi: 10.1016/j.jms.2021.111510.
[42] Ghysels M, Liu Q, Fleisher AJ, Hodges JT. A variable-temperature cavity ring-down spectrometer with application to line shape analysis of CO_2 spectra in the 1600 nm region. Appl Phys B 2017;123:1–13. Doi :10.1007/s00340-017-6686-y.
[43] Liu Q-H, Lv Y-N, Zou C-L, Cheng C-F, Hu S-M. Saturated absorption spectroscopy of HD at 76 K. Phys Rev A 2022;106:062805. Doi : 10.1103/PhysRevA.106.062805
[44] Kassi S, Romanini D, Campargue A. Mode by mode CW-CRDS at 80 K: application to the 1.58 µm transparency window of CH_4. Chem Phys Letters 2009;477:17–21. Doi: 10.1016/j.cplett.2009.06.097.
[45] Mondelain D, Kassi S, Sala T, Romanini D, Marangoni M, Campargue A. Sub-MHz accuracy measurement of the S(2) 2–0 transition frequency of D_2 by comb-assisted cavity ring down spectroscopy. J Mol Spectrosc 2016;326:5-8. Doi:10.1016/j.jms.2016.02.008.
[46] Mondelain D, Mikhailenko SN, Karlovets EV, Béguier S, Kassi S, Campargue A. Comb-Assisted Cavity Ring Down Spectroscopy of ^{17}O enriched waterbetween 7443 and 7921 cm^{-1}. J Quant Spectrosc Radiat Transf 2017;203:206-212. Doi:10.1016/j.jqsrt.2017.03.029.
[47] Burkart J, Romanini D, Kassi S. Optical feedback stabilized laser tuned by single-sideband modulation. Opt Lett 2013;38:2062-2064. Doi: 10.1364/OL.38.002062.
[48] Kassi S, Guessoum S, Abanto JCA, Tran H, Campargue A, Mondelain D. Temperature dependence of the collision-induced absorption band of O_2 near 1.27 µm. J Geophys Res Atm 2021;126:e2021JD034860. Doi : 10.1029/2021JD034860.
[49] Casado M, Stoltmann T, Landais A, Jobert N, Daëron M, Prié F, Kassi S. High stability in near-infrared spectroscopy: part 1, adapting clock techniques to optical feedback. Applied Physics B 2022;128:1-7. Doi: 10.1007/s00340-022-07774-2.
[50] Konefał M, Kassi S, Mondelain D, Campargue A. High sensitivity spectroscopy of the O_2 band at 1.27 µm: (I) pure O_2 line parameters above 7920 cm^{-1}. J Quant Spectrosc Radiat Transf 2020;241:106653. Doi :10.1016/j.jqsrt.2019.106653.
[51] Morville J, Romanini D, Chenevier M, Kachanov A. Effects of laser phase noise on the injection of a high-finesse cavity. Appl Opt 2002;41:6980. Doi : 10.1364/AO.41.006980.
[52] https://github.com/usnistgov/MATS. Doi:10.18434/M32200
[53] Gordon IE, Rothman LS, Hargreaves RJ, Hashemi R, Karlovets EV, Skinner FM, Conway EK, Hill C, Kochanov RV, Tan Y, Wcisło P, Finenko AA, Nelson K, Bernath PF, Birk M, Boudon V, Campargue A, Chance KV, Coustenis A, Drouin BJ, Flaud J-M, Gamache RR, Hodges JT, Jacquemart D, Mlawer EJ, Nikitin AV, Perevalov VI, Rotger M, Tennyson J, Toon GC, Tran H, Tyuterev VG, Adkins EM, Baker A, Barbe A, Canè E, Császár AG, Dudaryonok A, Egorov O, Fleisher AJ, Fleurbaey H, Foltynowicz A, Furtenbacher T, Harrison JJ, Hartmann J-M, Horneman V-M, Huang X, Karman T, Karns J, Kassi S, Kleiner I, Kofman V, Kwabia–Tchana F, Lavrentieva NN, Lee TJ, Long DA, Lukashevskaya AA, Lyulin OM, Makhnev VY, Matt W, Massie ST, Melosso M, Mikhailenko SN, Mondelain D, Müller HSP, Naumenko OV, Perrin A, Polyansky OL, Raddaoui E, Raston PL, Reed ZD, Rey M, Richard C, Tóbiás R, Sadiek I, Schwenke DW, Starikova E, Sung K, Tamassia F, Tashkun SA, Vander Auwera J, Vasilenko IA, Vigasin AA, Villanueva GL, Vispoel B, Wagner G, Yachmenev A, Yurchenko SN. The HITRAN2020 molecular spectroscopic database. J Quant Spectrosc Radiat Transf 2022; 277:107949. Doi: 10.1016/j.jqsrt.2021.107949.
[54] Birk M, Röske C, Wagner G. High accuracy CO_2 Fourier transform measurements in the range 6000–7000 cm^{-1}. J Quant Spectrosc Radiat Transf 2021;272:107791. Doi : 10.1016/j.jqsrt.2021.107791.
[55] Nikitin A V, Lyulin O M, Mikhailenko S N, Perevalov V I, Filippov N N, Grigoriev I M, Morino I, Yoshida Y, Matsunaga Y. GOSAT-2014 methane spectral line list, J Quant Spectrosc Radiat Transf 2015;154:63-71. Doi: 10.1016/j.jqsrt.2014.12.003.
[56] Rohart F, Mader H, Nicolaisen H-W. Speed dependence of rotational relaxation induced by foreign gas collisions: Studies on CH_3F by millimeter wave coherent transients. J Chem Phys 1994;101:6475–6486. Doi: 10.1063/1.468342
[57] Rohart F, Ellendt A, Kaghat F,Mader H. Self and polar foreign gas line broadening and frequency shifting of CH_3F: Effect of the speed dependence observed by millimeter-wave coherent transients. J Molec Spectrosc 1997;185:222–233. Doi: 10.1006/jmsp.1997.7395

[58] Gordon IE, Rothman LS, Hargreaves RJ, Hashemi R, Karlovets EV, Skinner FM, Conway EK, Hill C, Kochanov RV, Tan Y, Wcisło P, Finenko AA, Nelson K, Bernath PF, Birk M, Boudon V, Campargue A, Chance KV, Coustenis A, Drouin BJ, Flaud J-M, Gamache RR, Hodges JT, Jacquemart D, Mlawer EJ, Nikitin AV, Perevalov VI, Rotger M, Tennyson J, Toon GC, Tran H, Tyuterev VG, Adkins EM, Baker A, Barbe A, Canè E, Császár AG, Dudaryonok A, Egorov O, Fleisher AJ, Fleurbaey H, Foltynowicz A, Furtenbacher T, Harrison JJ, Hartmann J-M, Horneman V-M, Huang X, Karman T, Karns J, Kassi S, Kleiner I, Kofman V, Kwabia–Tchana F, Lavrentieva NN, Lee TJ, Long DA, Lukashevskaya AA, Lyulin OM, Makhnev VY, Matt W, Massie ST, Melosso M, Mikhailenko SN, Mondelain D, Müller HSP, Naumenko OV, Perrin A, Polyansky OL, Raddaoui E, Raston PL, Reed ZD, Rey M, Richard C, Tóbiás R, Sadiek I, Schwenke DW, Starikova E, Sung K, Tamassia F, Tashkun SA, Vander Auwera J, Vasilenko IA, Vigasin AA, Villanueva GL, Vispoel B, Wagner G, Yachmenev A, Yurchenko SN. The HITRAN2020 molecular spectroscopic database. J Quant Spectrosc Radiat Transf 2022; 277:107949. Doi: 10.1016/j.jqsrt.2021.107949.
[59] Armante R, Scott N, Crevoisier C, Capelle V, Crepeau L, Jacquinet N, Chédin A. Evaluation of spectroscopic databases through radiative transfer simulations compared to observations. Application to the validation of GEISA 2015 with IASI and TCCON. J Molec Spectrosc 2016;327:180–192. Doi: 10.1016/j.jms.2016.04.004